

Heat transfer and flow regimes in quasi-static magnetoconvection with a vertical magnetic field

Ming Yan¹, Michael A. Calkins¹, Stefano Maffei¹, Keith Julien², Steven M. Tobias³, and Philippe Marti⁴

¹Department of Physics, University of Colorado, Boulder, CO 80309, USA

²Department of Applied Mathematics, University of Colorado, Boulder, CO 80309, USA

³Department of Applied Mathematics, University of Leeds, Leeds, UK LS2 9JT

⁴Department of Earth Science, ETH Zurich

(Received xx; revised xx; accepted xx)

Numerical simulations of quasi-static magnetoconvection with a vertical magnetic field are carried out up to a Chandrasekhar number of $Q = 10^8$ over a broad range of Rayleigh numbers Ra . Three magnetoconvection regimes are identified: two of the regimes are magnetically-constrained in the sense that a leading-order balance exists between the Lorentz and buoyancy forces, whereas the third regime is characterized by unbalanced dynamics that is similar to non-magnetic convection. Each regime is distinguished by flow morphology, momentum and heat equation balances, and heat transport behavior. One of the magnetically-constrained regimes appears to represent an ‘ultimate’ magnetoconvection regime in the dual limit of asymptotically-large buoyancy forcing and magnetic field strength; this regime is characterized by an interconnected network of anisotropic, spatially-localized fluid columns aligned with the direction of the imposed magnetic field that remain quasi-laminar despite having large flow speeds. As for non-magnetic convection, heat transport is controlled primarily by the thermal boundary layer. Empirically, the scaling of the heat transport and flow speeds with Ra appear to be independent of the thermal Prandtl number within the magnetically-constrained, high- Q regimes.

1. Introduction

Convective heat transfer is a fundamental process that controls the thermal evolution of planets and stars (Miesch 2005; Jones 2011). In these natural systems the fluid is strongly forced, and thought to be in a turbulent state. Magnetic fields generated by the motion of electrically conducting fluids permeate many of these systems, and can have a significant influence on the dynamics via electromagnetic forces. Understanding such dynamics is crucial for determining how planets and stars evolve thermally over their lifetimes. However, the detailed role of strong magnetic fields in modifying the heat transport and dynamics remains poorly understood when the buoyancy forcing becomes large.

Rayleigh-Bénard convection is a canonical model for theoretical and numerical studies of buoyancy-driven flow that consists of a fluid layer contained between plane, parallel boundaries separated by a vertical distance H . A constant gravity vector $\mathbf{g} = -g\hat{\mathbf{z}}$ points vertically downward ($\hat{\mathbf{z}}$ is the vertical unit vector), and a constant temperature difference $\Delta T = T_{\text{bottom}} - T_{\text{top}} > 0$, is maintained to drive convection. For a Boussinesq fluid with thermal expansion coefficient α , kinematic viscosity ν , and thermal diffusivity

κ , convective motions are controlled by the Rayleigh number (Ra) and thermal Prandtl number (Pr),

$$Ra = \frac{g\alpha\Delta TH^3}{\nu\kappa}, \quad Pr = \frac{\nu}{\kappa}. \quad (1.1)$$

As the Rayleigh number becomes large, unconstrained convection is known to undergo a transition to turbulence, as characterized by a broad range of spatiotemporal scales (e.g. Ahlers *et al.* 2009; Lohse & Xia 2010; Chillà & Schumacher 2012).

When an externally-imposed, vertical magnetic field $\mathbf{B}_0 = \mathcal{B}\hat{\mathbf{z}}$ permeates the fluid layer, the convective dynamics also depends on the Chandrasekhar number (Q) and magnetic Prandtl number (Pm) defined as

$$Q = \frac{\mathcal{B}^2 H^2}{\rho\nu\mu\eta}, \quad Pm = \frac{\nu}{\eta}, \quad (1.2)$$

where $\mathcal{B} = |\mathbf{B}_0|$, ρ is the fluid density, μ is the vacuum permeability, and η is the magnetic diffusivity. The relative sizes of the thermal and magnetic Prandtl numbers control the time-dependence of the onset of convection; for fluids characterized by $Pr \geq Pm$, the onset of convection is steady, whereas oscillatory convection occurs when $Pr < Pm$ (Chandrasekhar 1961). The former relationship is relevant to liquid metals, including both planetary interiors (French *et al.* 2012; Pozzo *et al.* 2013) and laboratory experiments (e.g. Cioni *et al.* 2000; Aurnou & Olson 2001; Burr & Müller 2001; Gillet *et al.* 2007; Yanagisawa *et al.* 2010; King & Aurnou 2013, 2015; Vogt *et al.* 2018*b*). Stellar interiors composed of plasmas are typically characterized by $Pr < Pm$ (e.g. Ossendrijver 2003), so oscillatory convection is likely important in this context. In the present work we consider the magnetohydrodynamic quasi-static limit only; the induced magnetic field is asymptotically-small relative to the imposed magnetic field and, as a result, the onset of convection is always steady (Chandrasekhar 1961).

For an asymptotically-strong vertical magnetic field, $Q \rightarrow \infty$, it can be shown that, within a layer of infinite horizontal extent, the onset of (steady) convection is characterized by critical Rayleigh number $Ra_c \rightarrow O(\pi^2 Q)$ and critical horizontal wavenumber $k_c \rightarrow O(\frac{1}{2}(\pi^4 Q)^{1/6})$ (Chandrasekhar 1961; Matthews 1999). Thus, the presence of a vertical magnetic field acts to stabilize convection, and leads to anisotropic motions.

Strongly-forced nonlinear magnetoconvection (MC) with $Q \gg 1$ remains poorly understood, despite its relevance for natural systems. For instance, estimates for the magnetic field strength in the Earth's outer core range up to $Q \approx 10^{15}$ (e.g. Gillet *et al.* 2010). In contrast, laboratory experiments and numerical simulations have been limited to $Q \lesssim O(10^6)$ (Cioni *et al.* 2000; Aurnou & Olson 2001; Burr & Müller 2001; Tao *et al.* 1998; Cattaneo *et al.* 2003; Zürner *et al.* 2016; Yu *et al.* 2018; Liu *et al.* 2018). Both laboratory experiments (Aurnou & Olson 2001) and numerical simulations (Yu *et al.* 2018) have found a non-dimensional heat transport scaling of $Nu \sim (Ra/Q)^{1/2}$ for $Q \lesssim 10^3$, where Nu is the Nusselt number. In contrast, the experimental study of Burr & Müller (2001) suggests a $Nu \sim (Ra/Q)^{2/3}$ scaling for $Q \rightarrow \infty$, though accessible values of the Chandrasekhar number were limited to $Q \lesssim 10^3$. The experiments of Cioni *et al.* (2000) reached up to $Q = 3.93 \times 10^6$ and covered a broad range of supercritical Rayleigh numbers in which three heat transport regimes were observed (in order of increasing Ra): (1) a $Nu \sim (Ra/Q)$ regime (their regime I); (2) an intermediate regime (their regime III) in which the heat transport law varies continuously with increasing Ra ; and (3) a third regime (their regime II) in which $Nu \sim Ra^{0.43}Q^{-0.25}$.

Scaling predictions for the heat transport in MC have used Malkus's (1954) concept of a marginally stable thermal boundary layer (Bhattacharjee *et al.* 1991), and energetic

arguments (using the approach introduced by Grossmann & Lohse 2000) relying on a predominance of ohmic dissipation over viscous dissipation (Bhattacharyya 2006). These two assumptions both lead to a $Nu \sim (Ra/Q)$ heat transport scaling law as $Q \rightarrow \infty$. Interestingly, this scaling law is independent of the height of the domain H , and independent of all diffusion coefficients except the magnetic diffusivity. This latter property suggests that the heat transport scaling behavior is independent of Pr as $Q \rightarrow \infty$.

In the present work we carry out direct numerical simulations of quasi-static MC in the plane layer geometry with magnetic field strengths up to $Q = 10^8$. We find three unique MC regimes that can be distinguished by flow characteristics, force and heat equation balances, and heat transport (Nu) scalings. The first regime is reminiscent of linear convection, with cellular flow structures and a heat transport that increases rapidly but cannot be characterized by a single power-law scaling. The second regime is characterized by localized, quasi-laminar convection ‘columns’ that align with the imposed magnetic field and shows a $Nu \sim (Ra/Q)^\gamma$ scaling, but with a value of γ that increases toward unity with increasing Q . Thus, our findings indicate that the previously observed $Nu \sim (Ra/Q)^{1/2}$ and $Nu \sim (Ra/Q)^{2/3}$ scalings are *transitional* and limited to relatively small values of Q . A third MC regime is observed that is similar to non-magnetic convection in both flow structure and heat transport behavior; here the flow is observed to become broadband in structure. Our results suggest that quasi-static MC does not become turbulent provided the Lorentz force remains dominant – we refer to such states as ‘magnetically-constrained’. Thus, two magnetically-constrained regimes are identified, whilst the third regime might be characterized as ‘magnetically-influenced’.

2. Methods

We use the quasi-static magnetohydrodynamic approximation that is valid when the magnetic Reynolds number $Rm = PmRe \rightarrow 0$, where the hydrodynamic Reynolds number is defined as $Re = UL/\nu$ (U is a typical flow speed, L is a typical flow lengthscale) (e.g. Moffatt 1970). In particular, the magnitude of the induced magnetic field (\mathbf{b}) is smaller than the imposed field (\mathbf{B}_0) by $O(Rm)$, thus $\mathbf{b} \sim O(Rm\mathbf{B}_0)$; this model has been used by many previous investigations (e.g. Zürner *et al.* 2016; Yu *et al.* 2018; Liu *et al.* 2018). Using this limit, the non-dimensional governing equations are given by

$$\partial_t \mathbf{u} = \underbrace{\nabla^2 \mathbf{u}}_{F_v} - \underbrace{\mathbf{u} \cdot \nabla \mathbf{u}}_{F_a} + \underbrace{Q \partial_z \mathbf{b}}_{F_l} + \underbrace{\frac{Ra}{Pr} T' \hat{\mathbf{z}}}_{F_b} - \underbrace{\nabla \Pi}_{F_p}, \quad (2.1)$$

$$0 = \nabla^2 \mathbf{b} + \partial_z \mathbf{u}, \quad (2.2)$$

$$\left(\partial_t - \frac{1}{Pr} \nabla^2 \right) T' = -\mathbf{u} \cdot \nabla T' - u_z \partial_z \bar{T} + \partial_z (\overline{u_z T'}), \quad (2.3)$$

$$\left(\partial_t - \frac{1}{Pr} \partial_z^2 \right) \bar{T} = -\partial_z (\overline{u_z T'}), \quad (2.4)$$

$$\nabla \cdot \mathbf{u} = 0, \quad \nabla \cdot \mathbf{B} = 0, \quad (2.5)$$

$$\mathbf{B} = \hat{\mathbf{z}} + \mathbf{b}, \quad T = \bar{T} + T', \quad (2.6)$$

where \mathbf{u} is the velocity field, \mathbf{b} is the induced magnetic field, T is the temperature, \bar{T} is the horizontally-averaged (mean) temperature (where $\overline{(\cdot)}$ denotes a horizontal average), T' is the fluctuating temperature and Π is the reduced pressure. Each of the

forces present in the momentum equation (2.1) have been identified by the symbols below them for future reference in our results. The viscous force, advection, Lorentz force, buoyancy force and pressure gradient force are given by F_v , F_a , F_l , F_b and F_p , respectively. The horizontal and vertical components of inertia are denoted by $\partial_t u_h$ and $\partial_t u_z$, respectively, where $u_h = \sqrt{u_x^2 + u_y^2}$, u_x and u_y are the horizontal velocity components, and u_z is the vertical velocity component. The equations have been non-dimensionalized by the domain-scale viscous diffusion time H^2/ν , imposed magnetic field magnitude \mathcal{B} and temperature difference $\Delta\mathcal{T}$. The boundary conditions are stress-free, constant temperature, and electrically insulating.

The equations are solved using a standard toroidal-poloidal decomposition of the velocity and magnetic field such that the solenoidal conditions are satisfied exactly (e.g. Jones & Roberts 2000). A pseudo-spectral code is used for simulating the above equations with Fourier series in the horizontal dimensions and Chebyshev polynomials in the vertical dimension (Marti *et al.* 2016). Numerical resolutions using up to $1536 \times 1536 \times 192$ physical-space grid points are used to ensure that the flow is well-resolved; these resolutions allow for at least 8 vertical grid points within the thermal boundary layer. The non-linear terms are de-aliased with the standard 2/3-rule. The equations are discretized in time with a third-order implicit-explicit Runge-Kutta scheme (Spalart *et al.* 1991). In most of our simulations we use a Prandtl number of $Pr = 1$; however, additional simulations with $Pr = 0.025$, relevant to liquid metals, suggest that our findings are insensitive to Pr .

The horizontal dimensions of the system are scaled by the critical horizontal wavelength, λ_c . The Rayleigh number corresponding to the marginal stability of horizontal wavenumber k is given by (Chandrasekhar 1961)

$$Ra_m = \frac{\pi^2 + k^2}{k^2} [(\pi^2 + k^2)^2 + \pi^2 Q]. \quad (2.7)$$

The critical Rayleigh number Ra_c is the minimum value of Ra_m for a given value of Q , and is found by minimizing the above expression for all k to find the critical wavenumber k_c that satisfies the expression

$$2k_c^6 + 3\pi^2 k_c^4 = \pi^6 + \pi^4 Q, \quad (2.8)$$

where $\lambda_c = 2\pi/k_c$. For the majority of the simulations we use a domain with non-dimensional size $10\lambda_c \times 10\lambda_c \times 1$. However, as the Rayleigh number is increased, the horizontal dimensions of the system can be reduced while still providing accurate flow statistics. Horizontal dimensions of $5\lambda_c \times 5\lambda_c$ are used for our most extreme cases. Tests with different horizontal dimensions were used to ensure that computed statistics showed convergence.

Amongst the output quantities we analyzed the Nusselt number, Nu , and the Reynolds number, Re . The Nusselt number measures the efficiency of convective heat transfer in our simulations and is defined by

$$Nu = 1 + Pr \langle u_z T' \rangle, \text{eps} \quad (2.9)$$

where $T' = T - \bar{T}$, and $\langle \cdot \rangle$ denotes a volumetric and time average. The Reynolds number measures the typical flow speeds and, with our particular non-dimensionalization of the governing equations, is defined by

$$Re = \langle u_x^2 + u_y^2 + u_z^2 \rangle^{1/2}. \quad (2.10)$$

Details of the numerical simulations are provided in the Appendix.

3. Results

3.1. Flow regime characterization

Three primary dynamical regimes of MC are found, which we refer to as the cellular, columnar and turbulent regimes. Each regime is illustrated in Fig. 1, where each panel shows a simulation domain with aspect ratio $5\lambda_c \times 5\lambda_c \times 1$, where $\lambda_c \approx 0.22, 0.15$ and 0.73 , respectively, for the three different cases. Only the first two regimes are considered to be magnetically-constrained in the sense that the Lorentz force plays a leading-order role in the dynamics. Each regime can be uniquely identified by: (1) the scaling of the heat transport and flow speeds with buoyancy forcing; (2) the physical structure and spectral characteristics of the flows; and (3) the relative sizes of each term in the governing equations.

Figs. 2(a) and (b) show the Nusselt number (Nu) and Reynolds number (Re) versus the Rayleigh number (Ra) for all $Pr = 1$ cases. The non-magnetic ($Q = 0$) case is shown for comparison, along with the $Nu \sim Ra^{2/7}$ scaling typically found in studies using moderate Ra and $Pr = O(1)$ (e.g. Castaing *et al.* 1989) and the ‘free-fall’ scaling, $Re \sim Ra^{1/2}$. All of the MC cases show qualitatively similar behavior to each other in their functional dependence of Nu and Re on Ra . Figs. 2(c) and (d) show Nu and Re versus Ra/Ra_c , where the similarities between cases with different Q values and the asymptotic behaviors can be more clearly seen.

The first, cellular regime is characterized by the cellular structures reminiscent of linear convection, as illustrated in the visualizations of Fig. 1(a,b). In this regime, the heat transfer and flow speeds increase rapidly with increasing Ra , but with a slope that continuously decreases. The time-averaged mean temperature profile for a typical case in this regime is shown in Fig. 3(a). Here, convective nonlinearities remain weak and the characteristic scale of fluid motion remains dominated by the critical horizontal wavenumber, as illustrated in the kinetic energy spectra shown in Fig. 4.

When Ra is increased to $\simeq 4Ra_c$, the slope of the (Nu, Ra) and (Re, Ra) curves for each value of Q appear to approach a constant value over a wide range of Ra . We refer to this regime as ‘columnar’ because of the characteristic structure of the flow field shown in Fig. 1(c,d), which consists of a network of spatially-localized columns that span the depth of the layer. Flow speeds, as indicated by the Reynolds number in Fig. 2(b), become large in this regime in the sense that an equivalent $Q = 0$ case would yield a turbulent flow, yet the fluid remains quasi-laminar and coherent. The simulations show that the columnar regime occupies an increasing range of Ra as Q is increased. The spatial localization of the convection leads to a locally-flattened kinetic energy spectrum centered near the critical wavenumber ($k = 10$ for the case shown), as illustrated in Fig. 4. Within the columnar regime, Figs. 3(a) and 3(b) shows that the fluid interior becomes nearly isothermal and the thermal boundary layers are well-established.

As first observed by Cioni *et al.* (2000), the interior mean temperature gradient can be positive for some of the cases. A possible explanation for this reversed (stable) gradient is due to the vertical structure of the anisotropic columns, as illustrated in the vertical slice of the temperature in Fig. 5. A given convection column exhibits an asymmetric structure about $z = 0.5$; for instance, upwelling flow tends to be thin near the bottom boundary where flow converges, and broader near the upper boundary where flow diverges. Horizontally-averaging this flow structure results in a weakly-stable interior temperature profile. The columns act as an efficient heat transfer mechanism in the sense that heat is carried directly from boundary to boundary with limited horizontal mixing.

The third, turbulent MC regime is marked by a decrease in the slope of both the Nu (cf. Cioni *et al.* 2000) and Re scalings with Ra . Here the columns disappear and, as a

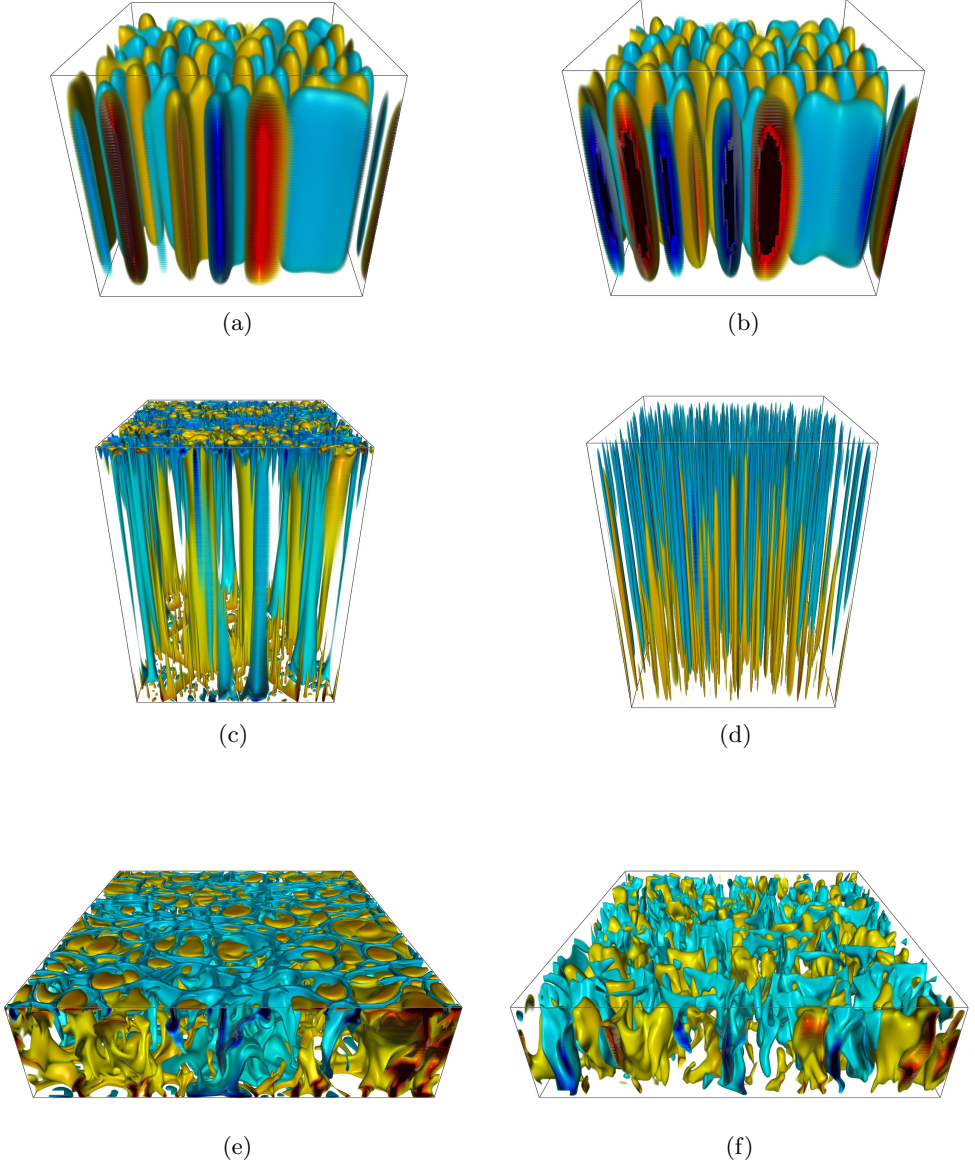


Figure 1: Volumetric renderings of the three magnetoconvection regimes identified in the present study. Isosurfaces of fluctuating temperature are shown in the first column [(a), (c), (e)]; isosurfaces of the vertical velocity are shown in the second column [(b), (d), (f)]. (a), (b) The cellular regime ($Q = 10^7$, $Ra = 1.3 \times 10^8$); (c), (d) the columnar regime ($Q = 10^8$, $Ra = 4 \times 10^{10}$); (e), (f) the turbulent regime ($Q = 10^4$, $Ra = 2 \times 10^7$). For all three cases, the Prandtl number is fixed at $Pr = 1$, and an aspect ratio of $5\lambda_c \times 5\lambda_c \times 1$ is shown, where λ_c is the critical wavelength (see main text for details).

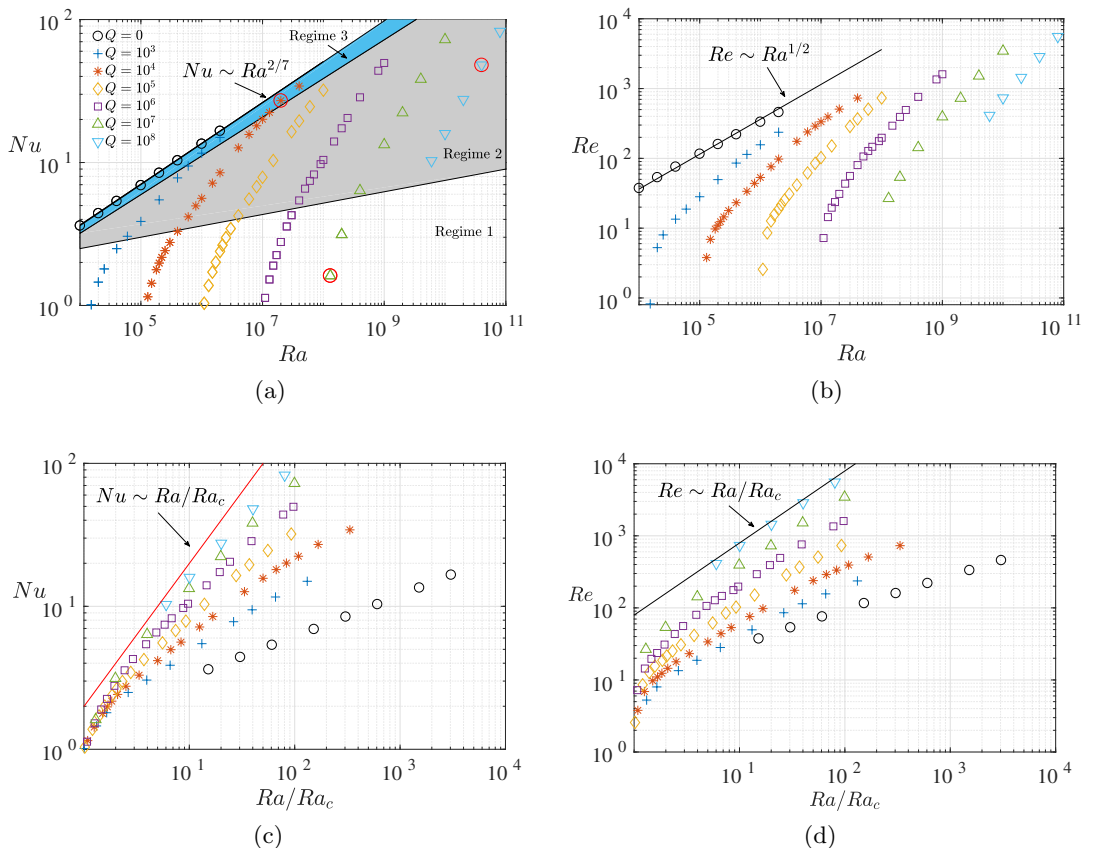


Figure 2: Heat transport and flow speeds in magnetoconvection. (a) Nusselt number versus Rayleigh number (cases shown in Fig. 1 and Fig. 9 are marked with a red circle); (b) Reynolds number versus Rayleigh number; (c) Nusselt number versus Ra/Ra_c ; (d) Reynolds number versus Ra/Ra_c . The three different regimes identified in the present study are illustrated in (a); regime 1 is the cellular regime, regime 2 is the columnar regime and regime 3 is the turbulent regime.

result, the flattened kinetic energy spectra observed in the columnar regime transition to a broader spectrum (Fig. 4) that is suggestive of a direct energy cascade and the development of an inertial subrange (the Kolmogorov spectrum $K(k) \sim k^{-5/3}$ is plotted for reference). However, the development of an inertial subrange is very slow and requires very large Ra . The Lorentz force still plays an important role in the dynamics, and extremely large Rayleigh numbers are required to leave the third regime and access flows in which the Lorentz force plays a negligible role.

3.2. The influence of the Prandtl number

A total of ten simulations with $Pr = 0.025$ have also been carried out to determine the dynamical influence of the thermal Prandtl number, and to compare with available data from laboratory experiments that use this same value of Pr . Specifically, we use $Q = 2 \times 10^6$ to compare with the results of Cioni *et al.* (2000) who used a cylindrical container filled with mercury. Fig. 6 shows the Cioni *et al.* (2000) data along with

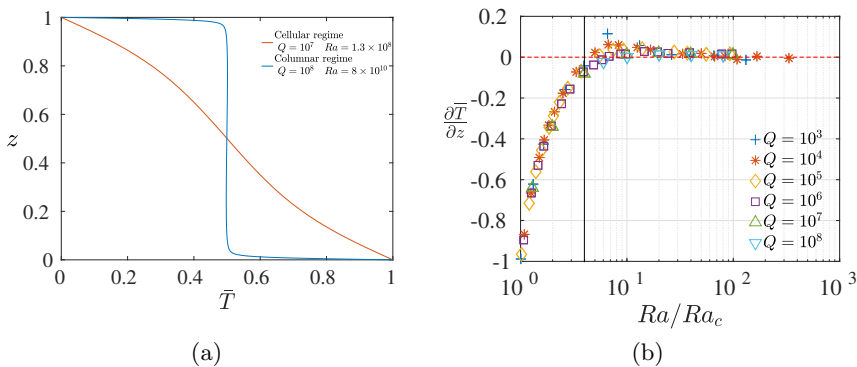


Figure 3: Characteristics of the time- and horizontally-averaged (mean) temperature ($Pr = 1$). (a) Mean temperature profiles for two representative cases within the cellular and columnar regimes. (b) Vertical gradient of the mean temperature at the vertical midplane. The solid black line roughly suggests the transition from the cellular regime to the columnar regime. The dashed red line indicates an isothermal interior.

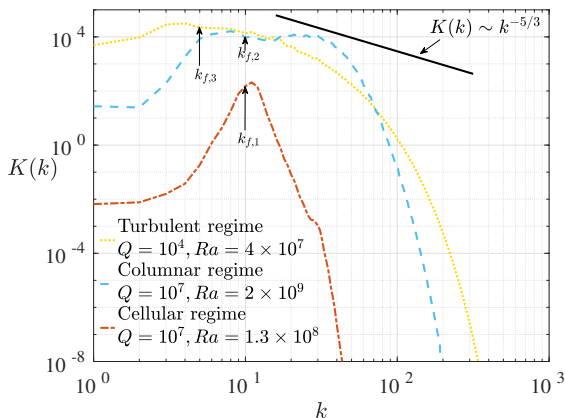


Figure 4: Instantaneous kinetic energy spectra, $K(k)$, from representative cases of the three different magnetoconvection regimes; spectra are computed at the vertical midplane ($z = 0$). The cellular regime is shown with the dash-dot line ($Q = 10^7, Ra = 1.3 \times 10^8$); the columnar regime is shown with the dashed line ($Q = 10^7, Ra = 2 \times 10^9$); and the turbulent regime is shown with the dotted line ($Q = 10^4, Ra = 4 \times 10^7$). $k_{f,1}$, $k_{f,2}$ and $k_{f,3}$ are the critical (forcing) wavenumbers for each case. The $k^{-5/3}$ slope is shown for reference.

the $Pr = 0.025$ and two $Pr = 1$ cases with comparable Q values (10^6 and 10^7) from the present work. In general, similar behavior is seen between the simulations and the experimental data, despite the differences in boundary conditions and geometry. As revealed by our results, the regime I of Cioni *et al.* (2000) actually consists of two distinct magnetically-constrained regimes (cellular and columnar) in which the flow cannot accurately be described as turbulent. Although they suggest a $Nu \sim Ra/Q$ fit to their data, our simulations show that this fit only arises at much higher values of Q . The

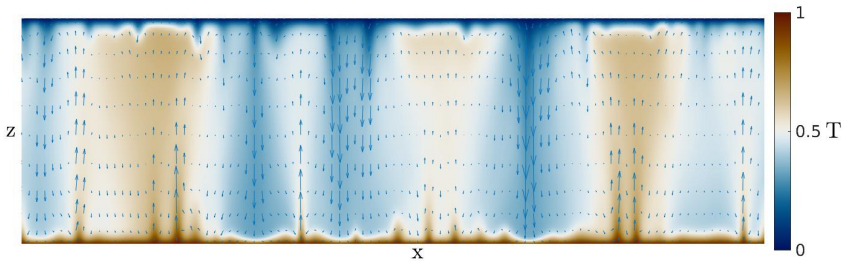


Figure 5: Two-dimensional (x, z) slice of temperature for a typical case in the magnetically-constrained columnar regime ($Q = 10^6$, $Ra = 1.5 \times 10^8$, $Pr = 1$), showing the broadening of thermal structures as hot (cold) fluid ascends (descends). The arrows indicate the velocity in the plane.

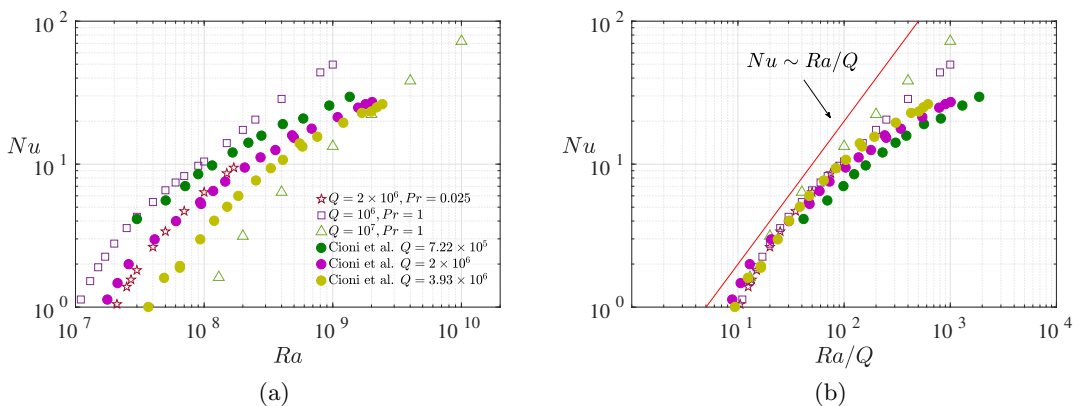


Figure 6: Comparison of simulation results with the $Pr = 0.025$ experimental data of Cioni *et al.* (2000). (a) Nusselt number versus Rayleigh number; (b) Nusselt number versus Ra/Q .

most significant discrepancies between the two datasets appear at higher values of Ra (or Ra/Q), where the Cioni *et al.* (2000) data shows a lower slope in comparison with the simulations (both $Pr = 0.025$ and $Pr = 1$). Because this difference is largest at higher values of Ra , it might be due to, as suggested by Cioni *et al.* (2000), the formation of a large-scale circulation in the experimental apparatus due to the eventual loss of magnetic constraint and flow anisotropy (Vogt *et al.* 2018a; Lim *et al.* 2019). Moreover, at the highest values of Ra accessed by Cioni *et al.* (2000) it is likely that the dynamics are within the third regime, within which different values of Pr might lead to different scaling behavior. Additional studies using the cylindrical geometry and higher values of Ra are necessary to quantify this effect in more detail.

We find that the Nu - Ra scaling behavior for $Pr = 0.025$ is nearly identical to that observed for the $Pr = 1$ cases, as shown in Fig. 6(b). In addition, we can identify the cellular and columnar regimes for the $Pr = 0.025$ cases based on the Nu scaling and flow structures. We note that single-mode MC dynamics are also Pr -independent (Matthews 1999; Julien *et al.* 1999). The mean temperature profiles in Fig. 7(a) show that the thickness of the thermal boundary layers observed in the $Pr = 0.025$ cases

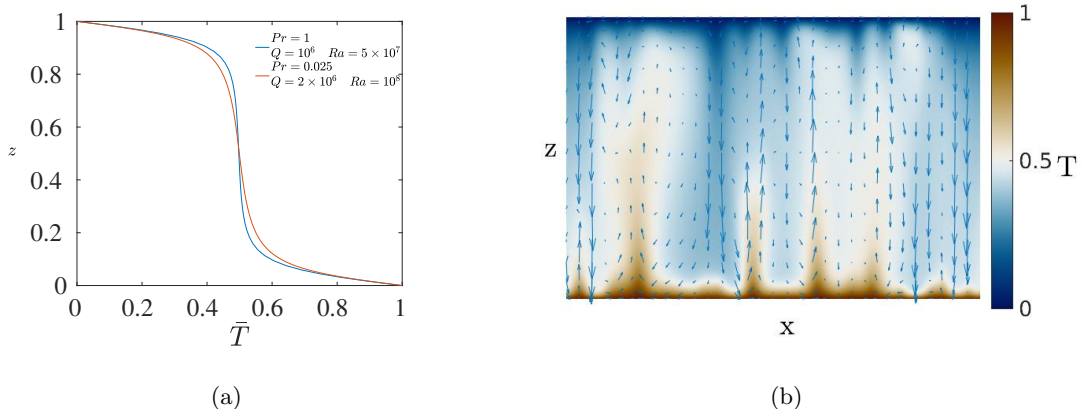


Figure 7: The influence of the thermal Prandtl number on magnetoconvection. (a) time- and horizontally-averaged (mean) temperature profile for cases with different Pr but the same Ra/Q ; (b) two-dimensional (x, z) slices of temperature for columnar regime with $Pr = 0.025$, ($Q = 2 \times 10^6$, $Ra = 1.7 \times 10^8$).

is comparable to the corresponding cases with $Pr = 1$ for a given value of Ra/Q . However, a larger interior temperature gradient is present for the $Pr = 0.025$ cases. Fig. 7 shows a two-dimensional (x, z) slice of the temperature field for a case in the columnar regime with $Pr = 0.025$. Both $Pr = 0.025$ and $Pr = 1$ cases show similar anisotropic columnar structures. However, as might be expected with a smaller Pr , heat diffuses to the surrounding fluid more rapidly before it is carried to the top of the layer. As a result, cases with a smaller Pr are expected to require a larger Ra/Ra_c to reach an isothermal interior for finite values of Q .

.eps

3.3. Balances

The magnetic interaction parameter, $N = \mathcal{B}^2 L / (\rho \mu \eta U)$ (where L and $U = |\mathbf{u}|$ are generic characteristic length and speed scales) can be used to estimate the relative magnitudes of the Lorentz force to the advection terms in the momentum equation (e.g. Davidson 2013). If one assumes that $L \equiv H$, we have $N = Q/Re$ (e.g. Cioni *et al.* 2000). In the present work, however, a definition that better captures the transition between the regimes identified above can be found by incorporating the Q -dependent horizontal length scale of the convective flows into the definition of the interaction parameter; we denote this rescaled interaction parameter by N_ℓ . From the vertical component of the momentum equation, for instance, we have

$$N_\ell \sim \frac{\text{Lorentz force}}{\text{advection}} \sim \frac{|Q \partial_z b_z|}{|u_z \partial_z u_z|} \sim Q \frac{|b_z|}{|u_z|^2} \sim Q \frac{|\ell^2|}{|u_z|} \sim \frac{Q^{2/3}}{Re}, \quad (3.1)$$

where, from the vertical component of the induction equation, we have used

$$b_z = -\nabla^{-2} \partial_z u_z \quad \Rightarrow \quad |b_z| \sim \ell^2 |u_z| = \ell^2 Re. \quad (3.2)$$

We assume $\ell \sim Q^{-1/6}$, vertical derivatives are of order one, and the vertical component of the velocity is asymptotically-larger than the horizontal components so that $u_z \sim Re$ (e.g. Matthews 1999). An identical relationship can be found from the horizontal components

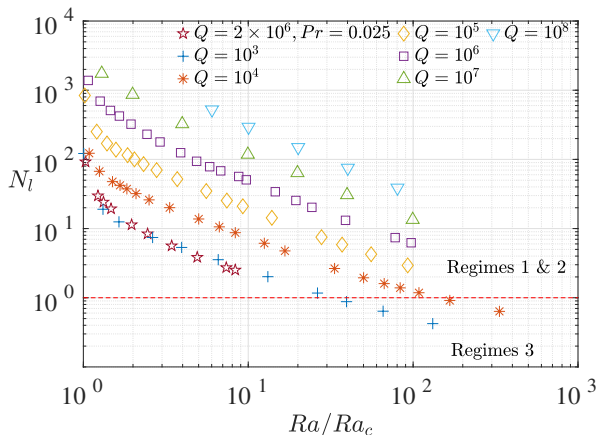


Figure 8: Rescaled interaction parameter $N_\ell = Q^{2/3}/Re$ versus Ra/Ra_c . The Lorentz force remains dominant provided $N_\ell \gtrsim 1$. The dashed red line shows the approximate location for the transition from the columnar regime to the turbulent regime. Unless explicitly stated all curves are for $Pr = 1$.

of the momentum equation by relating the horizontal and vertical velocity components through the continuity equation. Thus, the transition from the columnar regime to the turbulent regime is expected when $N_\ell \simeq 1$. Fig. 8 shows the interaction parameter N_ℓ plotted versus Ra/Ra_c . The dashed red line indicates the boundary between the columnar and turbulent regimes. It is suggested that with a larger Q value, a larger Ra/Ra_c is required to leave the columnar regime. The $Pr = 0.025$ data suggests that smaller values of Pr will yield a narrower (in terms of Ra) columnar regime, and a broader turbulent regime for a fixed value of Q .

Fig. 9 shows vertical profiles of the instantaneous horizontal rms of each term in the governing equations, for representative $Pr = 1$ cases in the cellular [(a)-(c)], columnar [(d)-(f)] and turbulent [(g)-(i)] regimes. Instantaneous values of the profiles are used to demonstrate that the force balances in the magnetically-constrained regimes apply at all times, and show remarkably smooth profiles; therefore, the choice of the particular instant in time does not affect the results. The interior and boundary layer are characterized by distinct balances, so it is helpful to consider the two regions separately. As predicted from the linear asymptotic scalings (e.g. Chandrasekhar 1961; Matthews 1999), Figs. 9(a), (b), (d) and (e) show that, for the cellular and columnar regimes, the leading-order force balance within the interior is between the Lorentz force (F_l), buoyancy force (F_b) and horizontal pressure gradient (F_p),

$$0 \approx Q\partial_z b_z + \frac{Ra}{Pr}T', \quad 0 \approx Q\partial_z b_h - \nabla_\perp \Pi \quad (\text{Regimes 1 and 2, interior}). \quad (3.3)$$

In the boundary layers we find that the pressure gradient balances the Lorentz force,

$$0 \approx Q\partial_z \mathbf{b} - \nabla \Pi, \quad (\text{Regimes 1 and 2, boundary layers}) \quad (3.4)$$

For the cellular regime, the vertical advection of the mean temperature and the horizontal diffusion terms are in dominant balance in the entire flow domain (cf. Matthews 1999),

$$u_z \partial_z \bar{T} \approx Pr^{-1} \nabla_\perp^2 T'. \quad (\text{Regime 1}) \quad (3.5)$$

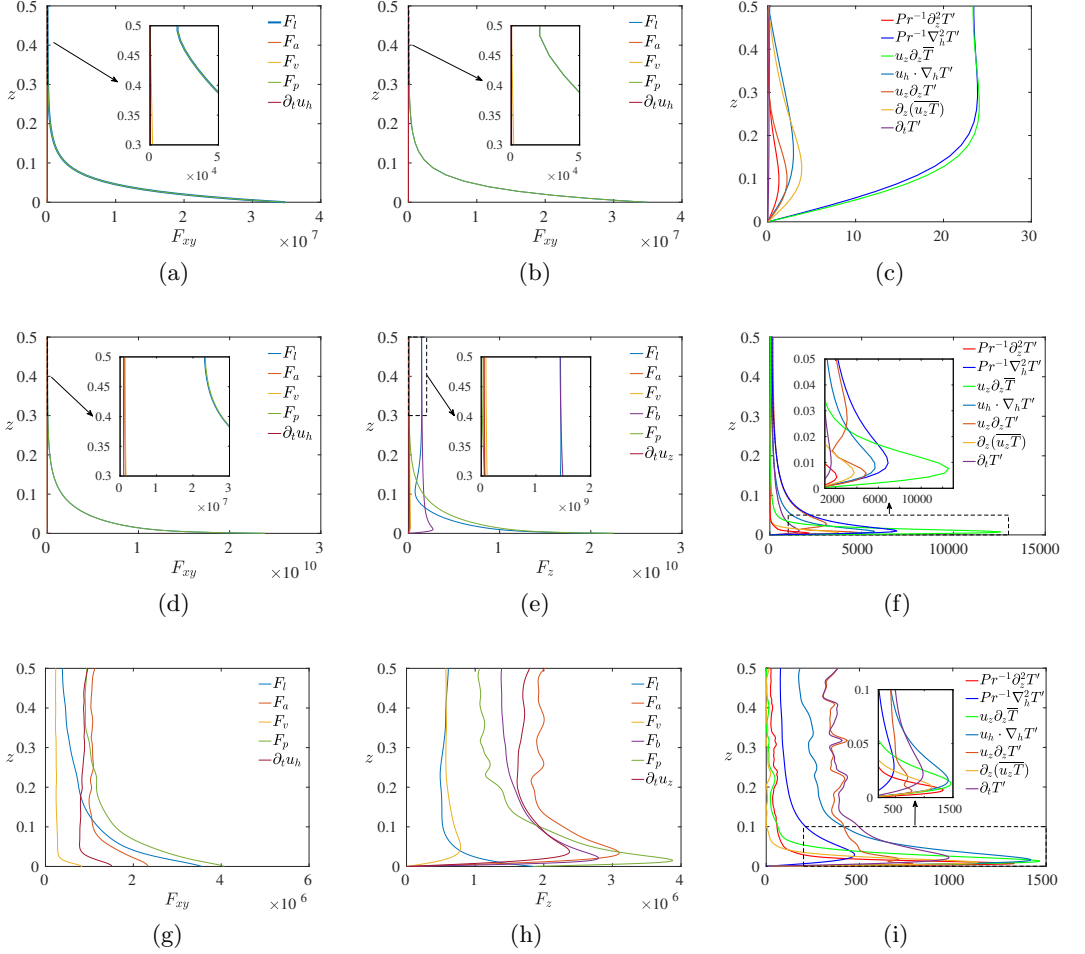


Figure 9: Instantaneous dynamical balances in $Pr = 1$ magnetoconvection. Vertical profiles of the horizontal rms of each term present in the momentum equation (2.1) [(a),(b),(d),(e),(g),(h)] and fluctuating heat equation (2.3) [(c),(f),(i)] are shown. The cellular regime ($Q = 10^7$, $Ra = 1.3 \times 10^8$): (a) horizontal forces $F_{xy} = (F_x^2 + F_y^2)^{1/2}$; (b) vertical forces F_z ; (c) all terms in the fluctuating heat equation. The columnar regime ($Q = 10^8$, $Ra = 4 \times 10^{10}$): (d) horizontal forces F_{xy} ; (e) vertical forces F_z ; (f) all terms in the fluctuating heat equation. The turbulent regime ($Q = 10^4$, $Ra = 2 \times 10^7$): (g) horizontal forces; (h) vertical forces; (i) all terms in the fluctuating heat equation. Vertical velocity, horizontal velocity, and horizontal gradient are given by u_z , $u_h = (u_x^2 + u_y^2)^{1/2}$ and $\nabla_h = (\partial_x, \partial_y, 0)$. Advection and the Lorentz, viscous, buoyancy and pressure gradient forces are denoted by F_a , F_l , F_v , F_b and F_p , respectively. Inertia in the horizontal and vertical components of the momentum equation are denoted by $\partial_t u_h$ and $\partial_t u_z$, respectively.

For the columnar regime, in the interior, the dominant terms in the fluctuating heat equation (2.3) are

$$\partial_t T' + u_z \partial_z T' \approx Pr^{-1} \nabla_{\perp}^2 T', \quad (\text{Regime 2, interior}) \quad (3.6)$$

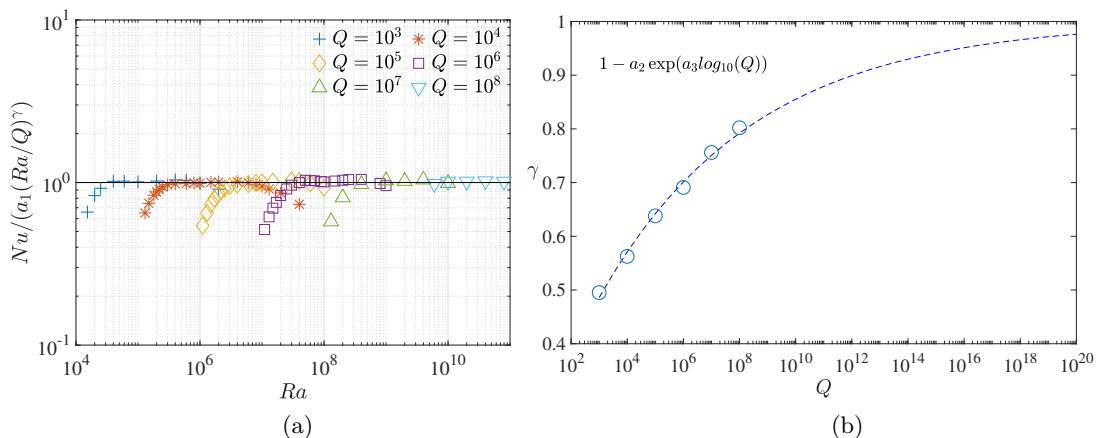


Figure 10: Power-law fits to the heat transport scaling within the columnar regime for $Pr = 1$. (a) The compensated Nusselt number, $Nu/(a_1(Ra/Q)^\gamma)$, versus the Rayleigh number, Ra , where $\gamma = 1 - a_2 \exp(a_3 \log_{10}(Q))$. (b) γ plotted versus Q . Here $a_1 = 0.4088$, $a_2 = 0.8847$, and $a_3 = -0.1810$.

whereas vertical advection of the mean temperature dominates in the boundary layers. The balance in the interior suggests that for a fixed value of Q , the horizontal length scale of the columns is, in addition to being strongly dependent upon Q , also limited by horizontal thermal diffusion.

In the turbulent regime [Fig. 9(d), (e) and (f)], the simulations show that advection, inertia, and the pressure gradient and buoyancy forces are important throughout the fluid layer. The turbulent regime possesses no instantaneous force balance in the sense that inertia and advection are dominant, whereas the Lorentz and viscous forces are subdominant. The heat equation is dominated by nonlinear advection within the interior, and all terms but horizontal diffusion play a significant role in the thermal boundary layer.

3.4. Power-law fits

The $Pr = 1$ heat transport data shown in Fig. 2(c) suggests that a power-law scaling of the form $Nu = a_1(Ra/Q)^\gamma$ (where a_1 is a constant) is present in the second, columnar regime, where γ appears to approach unity for increasing Q . Since γ increases with Q at a decreasing rate, we first compute γ in the columnar regime for individual Q values, then compute a least-squares fit of the form $\gamma = 1 - a_2 \exp(a_3 \log_{10}(Q))$, where a_2 and a_3 are constants. This latter exponential fit for γ has no physical basis and is meant only to provide a guide for the behavior at large values of Q . Fig. 10 (a) shows the rescaled, or compensated, Nusselt number, $Nu/(a_1(Ra/Q)^\gamma)$, plotted versus the Rayleigh number, Ra , with the fitting results: $a_1 = 0.4088$, $a_2 = 0.8847$, $a_3 = -0.1810$.

Fig. 10(b) shows in detail how γ changes with Q . The exponential fit suggests that γ reaches 0.95 around $Q = 10^{16}$, which is close to estimates for Q in the Earth's outer core (e.g. Gillet *et al.* 2010).

The flow speeds in the columnar regime can be understood by balancing the Lorentz force F_l and buoyancy force F_b in the vertical component of the momentum equation, such that

$$Q \partial_z b_z \approx (Ra/Pr) T' \quad \Rightarrow \quad Q b_z \sim (Ra/Pr) T', \quad (3.7)$$

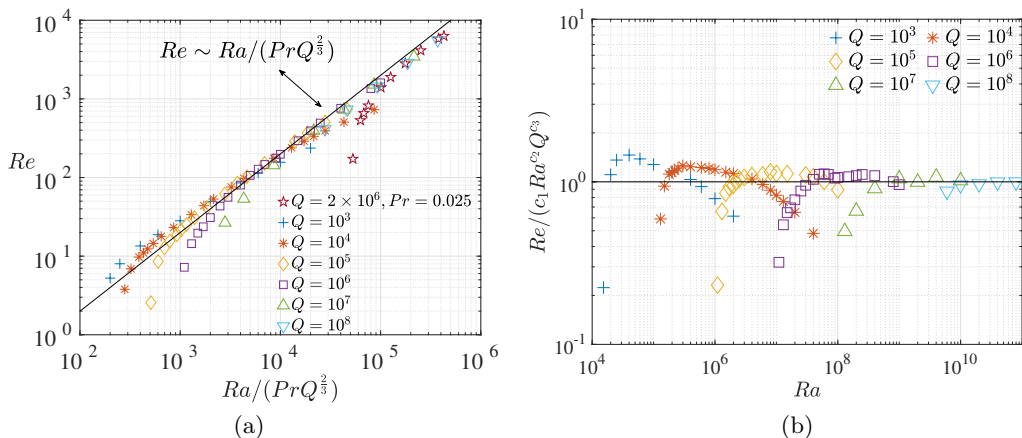


Figure 11: Power-law scaling for the Reynolds number. (a) The Reynolds number versus $Ra/(PrQ^{2/3})$. (b) The compensated Reynolds number, $Re/(c_1 Ra^{c_2} Q^{c_3})$, plotted versus the Rayleigh number, Ra . Here $c_1 = 0.0324$, $c_2 = 0.9542$, $c_3 = -0.6461$ are given by a least squares fitting of $Re = c_1 Ra^{c_2} Q^{c_3}$ applied to the Re data in the columnar regime.

where we again assume $\ell \sim Q^{-1/6}$, vertical derivatives are order one, $u_z \sim Re$ and $|b_z| \sim \ell^2 Re$. If we also assume a weak Q -dependence of T' we then have

$$Q\ell^2 Re \sim Ra/Pr \quad \Rightarrow \quad Re \sim Ra/(PrQ^{2/3}). \quad (3.8)$$

We emphasize that this magnetically-constrained scaling is steeper than the turbulent, free-fall scaling in which $Re \sim Ra^{1/2}$ due to the linearity of the balance. In Fig.11 (a) we show that this scaling collapses the data well in the columnar regime. A least squares fitting of $Re = c_1 Ra^{c_2} Q^{c_3}$ applied to the Re data in the columnar regime gives $c_1 = 0.0324$, $c_2 = 0.9542$, and $c_3 = -0.6461$. Fig.11 (b) shows the compensated Reynolds number, $c_1^{-1} Re Ra^{-c_2} Q^{-c_3}$, plotted versus Ra . As might be expected if one assumes an asymptotic state exists, the coefficients fit the data better as Q increases.

4. Conclusions

A systematic parameter survey of quasi-static magnetoconvection was carried out in a plane layer geometry. The results show three primary magnetoconvection regimes, with each regime distinguishable through unique heat transfer and convective-speed scalings, flow morphology, spectral characteristics, and dominant balances in the momentum and heat equations. For a fixed value of Q , and in order of increasing Rayleigh number, the first two regimes are characterized by a predominant Lorentz force and are therefore magnetically-constrained; the third regime is transitional and weakly-influenced by the Lorentz force. For large values of Q , the convective flow is highly-anisotropic in both the first (cellular) and second (columnar) regimes. The columnar regime is characterized by spatially-localized convective columns that span the fluid depth, and numerical analysis of the governing equations demonstrates that this regime is characterized by asymptotically-small advection and inertia, despite large Reynolds numbers.

Heat transport in the columnar regime is controlled by the thermal boundary layers and shows a power-law scaling with the Rayleigh number. Previous MC studies have suggested a $Nu \sim (Ra/Q)$ scaling for the $Q \rightarrow \infty$ limit. More generally, our simulations

suggest a scaling of the form $Nu \sim (Ra/Q)^\gamma$, with $\gamma \rightarrow 1$ as $Q \rightarrow \infty$. Thus, previous work finding $\gamma = 1/2$ (Aurnou & Olson 2001; Yu *et al.* 2018) and $\gamma = 2/3$ (Burr & Müller 2001) are transitional and observable only at relatively small values of Q .

For non-magnetic convection, the so-called ‘ultimate’ regime is a hypothetical state of convection in which the entire fluid layer is turbulent, and is thought to arise in the asymptotic limit of large Ra (Kraichnan 1962). Simulations of unconstrained convection in triply-periodic domains have shown that the ultimate regime may occur in the absence of thermal boundary layers (Lohse & Toschi 2003), and recent strongly-forced, two-dimensional simulations in a bounded domain also show a transition in heat transport that is indicative of an ultimate regime (Zhu *et al.* 2018). Laboratory experiments using internal heating also show evidence of reaching an ultimate regime (Lepot & Aumatre 2018). When additional forces are present that constrain the convection, regimes of flow that are fundamentally different from those in unconstrained convection can be realized. Our results suggest that the columnar regime represents an ultimate state for magnetically-constrained, quasi-static MC. Of course, the relatively limited accessible values of Q (and Ra) might hinder the ability to observe the $Nu \sim Ra/Q$ scaling that is thought to be indicative of this MC state, though our data suggests a trend toward this limit.

Finally, the Coriolis force, like the Lorentz force, can also act as a ‘constraint’ on convection that results in anisotropic flows. In contrast to MC, however, rotationally-constrained convection does exhibit a turbulent state, as observed with direct numerical simulation (e.g. Stellmach *et al.* 2014; Guervilly *et al.* 2014; Favier *et al.* 2014) and numerical simulation of an asymptotically-reduced equation set (Julien *et al.* 2012; Rubio *et al.* 2014). This difference may be due to the different energetic contributions that each of these two forces makes to convection, and to the different asymptotic scalings that characterize the two types of convection. While the Coriolis force has zero direct contribution to the energetics of rotating convection, the quasi-static Lorentz force is purely dissipative. Moreover, all three components of the velocity vector are of comparable magnitude in rotationally-constrained convection (Sprague *et al.* 2006), yet in MC the vertical component of the velocity vector is asymptotically-larger than the corresponding horizontal components that results in different asymptotic-ordering of the various forces in the momentum equation (Matthews 1999). In particular, in large- Q MC, the viscous force is asymptotically-larger than the inertial force, whereas these two terms are of the same asymptotic order in rotationally-constrained convection. Understanding how the Lorentz and Coriolis forces act in combination on convection is important in understanding magnetic field generation in stars and planets. Although numerical simulations have led to significant advances in our understanding of the role played by these two forces in convection (e.g. Yadav *et al.* 2016; Schaeffer *et al.* 2017; Aubert *et al.* 2017), it is currently unknown what ultimate state appears at high Rayleigh numbers, or if such a state exists at all.

Acknowledgements

This work was supported by the National Science Foundation under grant EAR #1620649 (MY, MAC, SM and KJ). SMT was supported by funding from the European Research Council (ERC) under the European Unions Horizon 2020 research and innovation program (agreement no. D5S-DLV-786780). This work utilized the RMACC Summit supercomputer, which is supported by the National Science Foundation (awards ACI-1532235 and ACI-1532236), the University of Colorado Boulder, and Colorado State University. The Summit supercomputer is a joint effort of the University of Colorado

Boulder and Colorado State University. The authors acknowledge the Texas Advanced Computing Center (TACC) at The University of Texas at Austin for providing high-performance computing resources that have contributed to the research results reported within this paper. Volumetric rendering was performed with the visualization software VAPOR (Clyne & Rast 2005; Clyne *et al.* 2007).

REFERENCES

- AHLERS, G., GROSSMANN, S. & LOHSE, D. 2009 Heat transfer and large scale dynamics in turbulent Rayleigh-Bénard convection. *Rev. Mod. Phys.* **81** (2), 503.
- AUBERT, JULIEN, GASTINE, THOMAS & FOURNIER, ALEXANDRE 2017 Spherical convective dynamos in the rapidly rotating asymptotic regime. *J. Fluid Mech.* **813**, 558–593.
- AURNOU, J. M. & OLSON, P. 2001 Experiments on Rayleigh-Bénard convection, magnetoconvection, and rotating magnetoconvection in liquid gallium. *J. Fluid Mech.* **430**, 283–307.
- BHATTACHARJEE, J. K., DAS, A. & BANERJEE, K. 1991 Turbulent Rayleigh-Bénard convection in a conducting fluid in a strong magnetic field. *Phys. Rev. A* **43** (2), 1097.
- BHATTACHARYYA, S. N. 2006 Scaling in magnetohydrodynamic convection at high Rayleigh number. *Phys. Rev. E* **74** (3), 035301.
- BURR, U. & MÜLLER, U. 2001 Rayleigh-Bénard in liquid metal layers under the influence of a vertical magnetic field. *Phys. Fluids* **13** (3247).
- CASTAING, B., GUNARATNE, G., HESLOT, F., KADANOFF, L., LIBCHABER, A., THOMAE, S., WU, X., ZALESKI, S. & ZANETTI, G. 1989 Scaling of hard thermal turbulence in Rayleigh-Bénard convection. *J. Fluid Mech.* **204**, 1–30.
- CATTANEO, F., EMONET, T. & WEISS, N. 2003 On the interaction between convection and magnetic fields. *Astrophys. J.* **588** (2), 1183.
- CHANDRASEKHAR, S. 1961 *Hydrodynamic and Hydromagnetic Stability*. U.K.: Oxford University Press.
- CHILLÀ, F & SCHUMACHER, J 2012 New perspectives in turbulent rayleigh-bénard convection. *Eur. Phys. J. E* **35** (7), 58.
- CIONI, S., CHAUMAT, S. & SOMMERIA, J. 2000 Effect of a vertical magnetic field on turbulent Rayleigh-Bénard convection. *Phys. Rev. E* **62** (4).
- CLYNE, J., MININNI, P., NORTON, A. & RAST, M. 2007 Interactive desktop analysis of high resolution simulations: application to turbulent plume dynamics and current sheet formation. *New J Phys* **9** (8), 301.
- CLYNE, J. & RAST, M. 2005 A prototype discovery environment for analyzing and visualizing terascale turbulent fluid flow simulations. In *Electronic Imaging 2005*, pp. 284–294. International Society for Optics and Photonics.
- DAVIDSON, P. A. 2013 *Turbulence in rotating, stratified and electrically conducting fluids*. Cambridge University Press.
- FAVIER, B., SILVERS, L. J. & PROCTOR, M. R. E. 2014 Inverse cascade and symmetry breaking in rapidly rotating Boussinesq convection. *Phys. Fluids* **26** (096605).
- FRENCH, M., BECKER, A., LORENZEN, W., NETTELMANN, N., BETHKENHAGEN, M, WICHT, J. & REDMER, R. 2012 Ab initio simulations for material properties along the Jupiter adiabat. *Astrophys. J. Supp. Ser.* **202** (1), 5.
- GILLET, N., BRITO, D., JAULT, D. & NATAF, H.-C. 2007 Experimental and numerical studies of magnetoconvection in a rapidly rotating spherical shell. *J. Fluid Mech.* **580**, 123–143.
- GILLET, N., JAULT, D., CANET, E. & FOURNIER, A. 2010 Fast torsional waves and strong magnetic field within the Earth's core. *Nature* **465**, 74–77.
- GROSSMANN, S. & LOHSE, D. 2000 Scaling in thermal convection: a unifying theory. *J. Fluid Mech.* **407**, 27–56.
- GUERVILLY, C., HUGHES, D. W. & JONES, C. A. 2014 Large-scale vortices in rapidly rotating Rayleigh-Bénard Convection. *J. Fluid Mech.* **758**, 407–435.
- JONES, C. A. 2011 Planetary magnetic fields and fluid dynamos. *Annu. Rev. Fluid Mech.* **43**, 583–614.
- JONES, C. A. & ROBERTS, P. H. 2000 Convection-driven dynamos in a rotating plane layer. *J. Fluid Mech.* **404**, 311–343.
- JULIEN, K., KNOBLOCH, E. & TOBIAS, S. M. 1999 Strongly nonlinear magnetoconvection in three dimensions. *Physica D* **128**, 105–129.
- JULIEN, K., RUBIO, A. M., GROOMS, I. & KNOBLOCH, E. 2012 Statistical and physical balances in low Rossby number Rayleigh-Bénard convection. *Geophys. Astrophys. Fluid Dyn.* **106** (4-5), 392–428.
- KING, E. M. & AURNOU, J. M. 2013 Turbulent convection in liquid metal with and without rotation. *Proc. Nat. Acad. Sci.* pp. 6688–6693.

- KING, E. M. & AURNOU, J. M. 2015 Magnetostrophic balance as the optimal state for turbulent magnetoconvection. *Proc. Nat. Acad. Sci.* **112** (4), 990–994.
- KRAICHNAN, R. H. 1962 Turbulent thermal convection at arbitrary Prandtl number. *Phys. Fluids* **5** (11), 1374–1389.
- LEPOT, S. & AUMATRE, S. AND GALLET, B. 2018 Radiative heating achieves the ultimate regime of thermal convection. *Proc. Natl. Acad. Sci.* **115**, 201806823.
- LIM, Z. L., CHONG, K. L., DING, G. & XIA, K. 2019 Quasistatic magnetoconvection: Heat transport enhancement and boundary layer crossing. *arXiv preprint arXiv:1902.08754*.
- LIU, W., KRASNOV, D. Y & SCHUMACHER, J. 2018 Wall modes in magnetoconvection at high hartmann numbers. *J. Fluid Mech.* **849**.
- LOHSE, D. & TOSCHI, F. 2003 Ultimate state of thermal convection. *Phys. Rev. Lett.* **90** (3), 034502.
- LOHSE, D. & XIA, K. 2010 Small-scale properties of turbulent rayleigh-bénard convection. *Annu. Rev. Fluid Mech.* **42**.
- MALKUS, W. V. 1954 The heat transport and spectrum of thermal turbulence. *Proc. R. Soc. Lond. A* **225** (1161), 196–212.
- MARTI, P., CALKINS, M. A. & JULIEN, K. 2016 A computationally efficient spectral method for modeling core dynamics. *Geochem. Geophys. Geosys.* **17** (8), 3031–3053.
- MATTHEWS, P. C. 1999 Asymptotic solutions for nonlinear magnetoconvection. *J. Fluid Mech.* **387**, 397–409.
- MIESCH, M. S. 2005 Large-scale dynamics of the convection zone and tachocline. *Living Rev. Sol. Phys.* **2** (1).
- MOFFATT, H. K. 1970 Turbulent dynamo action at low magnetic Reynolds number. *J. Fluid Mech.* **41**, 435–452.
- OSSENDRIJVER, M. 2003 The solar dynamo. *Astron. Astrophys. Rev.* **11** (4), 287–367.
- POZZO, M., DAVIES, C. J., GUBBINS, D. & ALFÉ, D. 2013 Transport properties for liquid silicon-oxygen-iron mixtures at Earth’s core conditions. *Phys. Rev. B* **87**, 014110.
- RUBIO, A. M., JULIEN, K., KNOBLOCH, E. & WEISS, J. B. 2014 Upscale energy transfer in three-dimensional rapidly rotating turbulent convection. *Phys. Rev. Lett.* **112**, 144501.
- SCHAEFFER, N., JAULT, D., NATAF, H.-C. & FOURNIER, A. 2017 Geodynamo simulations with vigorous convection and low viscosity. *Geophys. J. Int.*, <https://arxiv.org/abs/1701.01299>, arXiv: 1701.01299.
- SPALART, P. R., MOSER, R. D. & ROGERS, M. M. 1991 Spectral methods for the Navier-Stokes equations with one infinite and two periodic directions. *J. Comp. Phys.* **96**, 297–324.
- SPRAGUE, M., JULIEN, K., KNOBLOCH, E. & WERNE, J. 2006 Numerical simulation of an asymptotically reduced system for rotationally constrained convection. *J. Fluid Mech.* **551**, 141–174.
- STELLMACH, S., LISCHPER, M., JULIEN, K., VASIL, G., CHENG, J. S., RIBEIRO, A., KING, E. M. & AURNOU, J. M. 2014 Approaching the asymptotic regime of rapidly rotating convection: boundary layers versus interior dynamics. *Phys. Rev. Lett.* **113**, 254501.
- TAO, L., WEISS, NO, BROWNJOHN, DP & PROCTOR, MRE 1998 Flux separation in stellar magnetoconvection. *Astrophys. J. Lett.* **496** (1), L39.
- VOGT, T., HORN, S., GRANNAN, A. M. & AURNOU, J. M. 2018a Jump rope vortex in liquid metal convection. *Proc. Natl. Acad. Sci.* **115** (50), 12674–12679.
- VOGT, TOBIAS, ISHIMI, WATARU, YANAGISAWA, TAKATOSHI, TASAKA, YUJI, SAKURABA, ATARU & ECKERT, SVEN 2018b Transition between quasi-two-dimensional and three-dimensional Rayleigh-Bénard convection in a horizontal magnetic field. *Phys. Rev. Fluids* **3** (1), 013503.
- YADAV, R. K., GASTINE, T. & CHRISTENSEN, U. R. 2016 Approaching a realistic force balance in geodynamo simulations. *Proc. Nat. Acad. Sci.* **113** (43), 12065–12070.
- YANAGISAWA, T., YAMAGISHI, Y., HAMANO, Y., TASAKA, Y., YOSHIDA, M., YANO, K. & TAKEDA, Y. 2010 Structure of large-scale flows and their oscillation in the thermal convection of liquid gallium. *Phys. Rev. E* **82** (016320).
- YU, X., ZHANG, J. & NI, M. 2018 Numerical simulation of the Rayleigh-Bénard convection under the influence of magnetic fields. *Int. J. Heat Mass Tran.* **120**, 1118–1131.
- ZHU, X., MATHAI, V., STEVENS, R. J., VERZICCO, R. & LOHSE, D. 2018 Transition to the ultimate regime in two-dimensional Rayleigh-Bénard convection. *Phys. Rev. Lett.* **120** (14), 144502.

ZÜRNER, T., LIU, W., KRASNOV, D. & SCHUMACHER, J. 2016 Heat and momentum transfer for magnetoconvection in a vertical external magnetic field. *Phys. Rev. E* **94** (4), 043108.

Appendix

Here we provide tables with details of the numerical simulations.

case	Q	Ra	Nu	Re	Δt	$N_x \times N_y \times N_z$
a1	0	1×10^4	3.62 ± 0.03	37.46 ± 0.22	5×10^{-4}	$384 \times 384 \times 48$
a2	0	2×10^4	4.41 ± 0.04	53.49 ± 0.38	2×10^{-4}	$384 \times 384 \times 96$
a3	0	4×10^4	5.37 ± 0.05	75.77 ± 0.59	5×10^{-5}	$768 \times 768 \times 96$
a4	0	1×10^5	6.93 ± 0.05	115.99 ± 0.67	5×10^{-5}	$768 \times 768 \times 96$
a5	0	2×10^5	8.46 ± 0.06	159.69 ± 0.52	5×10^{-5}	$768 \times 768 \times 96$
a6	0	4×10^5	10.34 ± 0.07	220.35 ± 0.86	2×10^{-5}	$768 \times 768 \times 96$
a7*	0	1×10^6	13.51 ± 0.14	333.47 ± 2.84	5×10^{-6}	$768 \times 768 \times 144$
a8*	0	2×10^6	16.62 ± 0.13	458.52 ± 3.11	5×10^{-7}	$1296 \times 1296 \times 144$

Table 1: **Details of the RBC cases.** Δt is the timestep size. $N_x \times N_y \times N_z$ denotes the spatial resolution. The box ratio is $10\lambda_c \times 10\lambda_c \times 1$ in cases without *, and $5\lambda_c \times 5\lambda_c \times 1$ in cases with * above. The horizontal wavenumber $k_c = 2.2215$.

case	Q	Ra	Nu	Re	Δt	$N_x \times N_y \times N_z$
b1	10^3	1.53×10^4	$1.01 \pm 0.00^*$	$0.82 \pm 0.00^*$	2×10^{-3}	$96 \times 96 \times 48$
b2	10^3	2×10^4	$1.46 \pm 0.00^*$	$5.26 \pm 0.00^*$	2×10^{-3}	$96 \times 96 \times 48$
b3	10^3	2.5×10^4	1.80 ± 0.01	8.00 ± 0.10	1×10^{-3}	$144 \times 144 \times 48$
b4	10^3	4×10^4	2.50 ± 0.02	13.45 ± 0.24	5×10^{-4}	$144 \times 144 \times 48$
b5	10^3	6×10^4	3.05 ± 0.02	18.74 ± 0.31	2×10^{-4}	$192 \times 192 \times 72$
b6	10^3	1×10^5	3.87 ± 0.03	28.18 ± 0.32	1×10^{-4}	$288 \times 288 \times 144$
b7	10^3	2×10^5	5.48 ± 0.05	49.60 ± 0.70	4×10^{-5}	$288 \times 288 \times 144$
b8	10^3	4×10^5	7.80 ± 0.08	85.55 ± 1.02	2×10^{-5}	$384 \times 384 \times 144$
b9	10^3	6×10^5	9.45 ± 0.10	113.97 ± 1.34	2×10^{-5}	$384 \times 384 \times 144$
b10	10^3	1×10^6	11.62 ± 0.13	156.48 ± 1.39	1×10^{-5}	$576 \times 576 \times 144$
b11	10^3	2×10^6	14.97 ± 0.14	236.63 ± 1.96	1×10^{-5}	$576 \times 576 \times 144$

Table 2: **Details of the $Q = 10^3$ cases.** Δt is the timestep size. $N_x \times N_y \times N_z$ denotes the spatial resolution. The box ratio is $10\lambda_c \times 10\lambda_c \times 1$. The horizontal wavenumber $k_c = 5.6842$. The case with $\pm 0.00^*$ indicates that it is just above critical Rayleigh and has a stable Nu or Re .

case	Q	Ra	Nu	Re	Δt	$N_x \times N_y \times N_z$
c1	10^4	1.3×10^5	1.149 ± 0.002	3.79 ± 0.02	1×10^{-4}	$96 \times 96 \times 48$
c2	10^4	1.5×10^5	1.43 ± 0.01	6.91 ± 0.10	1×10^{-4}	$96 \times 96 \times 48$
c3	10^4	1.8×10^5	1.78 ± 0.01	9.74 ± 0.09	1×10^{-4}	$96 \times 96 \times 48$
c4	10^4	2×10^5	1.98 ± 0.01	11.01 ± 0.20	1×10^{-4}	$192 \times 192 \times 48$
c5	10^4	2.2×10^5	2.17 ± 0.01	12.38 ± 0.24	1×10^{-4}	$192 \times 192 \times 48$
c6	10^4	2.5×10^5	2.42 ± 0.02	14.51 ± 0.28	1×10^{-4}	$192 \times 192 \times 48$
c7	10^4	3×10^5	2.76 ± 0.02	17.85 ± 0.36	1×10^{-4}	$192 \times 192 \times 48$
c8	10^4	4×10^5	3.30 ± 0.04	23.15 ± 0.86	5×10^{-5}	$192 \times 192 \times 48$
c9	10^4	6×10^5	4.17 ± 0.05	33.74 ± 0.87	5×10^{-5}	$192 \times 192 \times 48$
c10	10^4	8×10^5	4.97 ± 0.05	43.84 ± 1.02	5×10^{-5}	$288 \times 288 \times 48$
c11	10^4	1×10^6	5.62 ± 0.04	53.26 ± 0.96	5×10^{-5}	$288 \times 288 \times 48$
c12	10^4	1.5×10^6	7.17 ± 0.04	75.72 ± 0.88	2×10^{-5}	$288 \times 288 \times 48$
c13	10^4	2×10^6	8.48 ± 0.05	97.62 ± 1.35	2×10^{-5}	$384 \times 384 \times 48$
c14	10^4	4×10^6	12.66 ± 0.09	175.40 ± 1.89	2×10^{-5}	$576 \times 576 \times 72$
c15	10^4	6×10^6	15.71 ± 0.10	238.97 ± 2.04	5×10^{-6}	$768 \times 768 \times 72$
c16*	10^4	8×10^6	18.07 ± 0.23	289.83 ± 3.26	4×10^{-6}	$576 \times 576 \times 96$
c17*	10^4	1×10^7	20.07 ± 0.33	333.93 ± 3.48	2×10^{-6}	$576 \times 576 \times 144$
c18*	10^4	1.3×10^7	22.40 ± 0.33	382.81 ± 5.97	1×10^{-6}	$576 \times 576 \times 144$
c19*	10^4	2×10^7	27.09 ± 0.35	507.76 ± 9.77	2×10^{-7}	$768 \times 768 \times 192$
c20*	10^4	4×10^7	34.27 ± 0.37	730.47 ± 8.33	1×10^{-7}	$1152 \times 1152 \times 288$

Table 3: **Details of the $Q = 10^4$ cases.** Δt is the timestep size. $N_x \times N_y \times N_z$ denotes the spatial resolution. The box ratio is $10\lambda_c \times 10\lambda_c \times 1$ in cases without *, and $5\lambda_c \times 5\lambda_c \times 1$ in cases with * above. The horizontal wavenumber $k_c = 8.6062$.

case	Q	Ra	Nu	Re	Δt	$N_x \times N_y \times N_z$
d1	10^5	1.1×10^6	$1.04 \pm 0.00^*$	2.57 ± 0.02	2×10^{-5}	$96 \times 96 \times 48$
d2	10^5	1.3×10^6	1.384 ± 0.001	8.56 ± 0.05	2×10^{-5}	$96 \times 96 \times 48$
d3	10^5	1.5×10^6	1.717 ± 0.002	12.70 ± 0.14	2×10^{-5}	$96 \times 96 \times 48$
d4	10^5	1.7×10^6	2.01 ± 0.01	15.58 ± 0.23	2×10^{-5}	$96 \times 96 \times 48$
d5	10^5	2×10^6	2.39 ± 0.01	18.71 ± 0.39	2×10^{-5}	$96 \times 96 \times 48$
d6	10^5	2.2×10^6	2.64 ± 0.02	21.51 ± 0.23	2×10^{-5}	$96 \times 96 \times 48$
d7	10^5	2.5×10^6	2.98 ± 0.02	25.21 ± 0.51	2×10^{-5}	$192 \times 192 \times 48$
d8	10^5	3×10^6	3.45 ± 0.02	30.76 ± 0.48	2×10^{-5}	$192 \times 192 \times 48$
d9	10^5	4×10^6	4.24 ± 0.04	41.51 ± 0.82	2×10^{-5}	$192 \times 192 \times 48$
d10	10^5	6×10^6	5.55 ± 0.05	61.80 ± 1.00	1×10^{-5}	$288 \times 288 \times 72$
d11	10^5	8×10^6	6.77 ± 0.05	84.85 ± 1.85	5×10^{-6}	$384 \times 384 \times 72$
d12	10^5	1×10^7	7.88 ± 0.05	102.51 ± 1.47	5×10^{-6}	$384 \times 384 \times 72$
d13	10^5	1.5×10^7	10.33 ± 0.07	150.78 ± 2.33	5×10^{-6}	$384 \times 384 \times 72$
d14	10^5	3×10^4	16.42 ± 0.07	286.82 ± 3.26	5×10^{-6}	$576 \times 576 \times 72$
d15	10^5	4×10^7	19.53 ± 0.08	367.83 ± 4.27	5×10^{-6}	$576 \times 576 \times 96$
d16	10^5	6×10^7	24.56 ± 0.11	506.18 ± 4.78	2×10^{-6}	$768 \times 768 \times 96$
d17	10^5	1×10^8	32.04 ± 0.12	733.46 ± 5.79	5×10^{-7}	$1152 \times 1152 \times 144$

Table 4: **Details of the $Q = 10^5$ cases.** Δt is the timestep size. $N_x \times N_y \times N_z$ denotes the spatial resolution. The box ratio is $10\lambda_c \times 10\lambda_c \times 1$. The horizontal wavenumber $k_c = 12.8343$. The case with $\pm 0.00^*$ indicates that it is just above critical Rayleigh and has a stable Nu or Re .

case	Q	Ra	Nu	Re	Δt	$N_x \times N_y \times N_z$
e1	10^6	1.1×10^7	1.135 ± 0.001	7.22 ± 0.02	2×10^{-6}	$96 \times 96 \times 48$
e2	10^6	1.3×10^7	1.518 ± 0.002	14.4 ± 0.10	2×10^{-6}	$96 \times 96 \times 48$
e3	10^6	1.5×10^7	1.898 ± 0.004	19.63 ± 0.16	2×10^{-6}	$96 \times 96 \times 48$
e4	10^6	1.7×10^7	2.255 ± 0.004	23.64 ± 0.16	2×10^{-6}	$144 \times 144 \times 48$
e5	10^6	2×10^7	2.78 ± 0.004	30.95 ± 0.19	2×10^{-6}	$144 \times 144 \times 48$
e6	10^6	2.5×10^7	3.5 ± 0.006	43.35 ± 0.20	2×10^{-6}	$192 \times 192 \times 48$
e7	10^6	3×10^7	4.28 ± 0.02	55.99 ± 0.17	2×10^{-6}	$192 \times 192 \times 48$
e8	10^6	4×10^7	5.43 ± 0.02	80.13 ± 0.34	2×10^{-6}	$192 \times 192 \times 48$
e9	10^6	5×10^7	6.56 ± 0.02	106.47 ± 0.35	2×10^{-6}	$288 \times 288 \times 48$
e10	10^6	6×10^7	7.43 ± 0.03	127.64 ± 0.34	2×10^{-6}	$288 \times 288 \times 48$
e11	10^6	7×10^7	8.25 ± 0.05	146.50 ± 0.85	2×10^{-6}	$384 \times 384 \times 48$
e12	10^6	9×10^7	9.74 ± 0.04	176.64 ± 1.03	2×10^{-6}	$384 \times 384 \times 48$
e13	10^6	1×10^8	10.43 ± 0.06	197.42 ± 1.72	2×10^{-6}	$384 \times 384 \times 48$
e14	10^6	1.5×10^8	14.03 ± 0.07	293.64 ± 2.35	2×10^{-6}	$384 \times 384 \times 48$
e15	10^6	2×10^8	17.36 ± 0.07	392.51 ± 3.53	2×10^{-6}	$576 \times 576 \times 72$
e16	10^6	2.5×10^8	20.49 ± 0.09	493.42 ± 4.08	1×10^{-6}	$576 \times 576 \times 96$
e17	10^6	4×10^8	28.58 ± 0.09	760.12 ± 7.85	1×10^{-6}	$768 \times 768 \times 96$
e18	10^6	8×10^8	43.83 ± 0.13	$1.35 \times 10^3 \pm 8.15$	5×10^{-7}	$1152 \times 1152 \times 144$
e19	10^6	1×10^9	49.70 ± 0.16	$1.60 \times 10^3 \pm 7.92$	2×10^{-7}	$1536 \times 1536 \times 144$

Table 5: **Details of the $Q = 10^6$ cases.** Δt is the timestep size. $N_x \times N_y \times N_z$ denotes the spatial resolution. The box ratio is $10\lambda_c \times 10\lambda_c \times 1$. The horizontal wavenumber $k_c = 18.9823$.

case	Q	Ra	Nu	Re	Δt	$N_x \times N_y \times N_z$
f1	10^7	1.3×10^8	1.615 ± 0.002	26.65 ± 0.11	2×10^{-7}	$192 \times 192 \times 48$
f2	10^7	2×10^8	3.124 ± 0.01	53.66 ± 0.48	2×10^{-7}	$192 \times 192 \times 48$
f3	10^7	4×10^8	6.37 ± 0.03	142.80 ± 1.28	2×10^{-7}	$192 \times 192 \times 48$
f4	10^7	1×10^9	13.33 ± 0.05	393.95 ± 2.38	2×10^{-7}	$384 \times 384 \times 96$
f5	10^7	2×10^9	22.29 ± 0.07	727.46 ± 5.54	2×10^{-7}	$576 \times 576 \times 96$
f6	10^7	4×10^9	38.26 ± 0.07	$1.51 \times 10^3 \pm 7.16$	2×10^{-7}	$768 \times 768 \times 144$
f7	10^7	1×10^{10}	72.40 ± 0.13	$3.45 \times 10^3 \pm 11.77$	5×10^{-8}	$1536 \times 1536 \times 192$

Table 6: **Details of the $Q = 10^7$ cases.** Δt is the timestep size. $N_x \times N_y \times N_z$ denotes the spatial resolution. The box ratio is $10\lambda_c \times 10\lambda_c \times 1$. The horizontal wavenumber $k_c = 27.9622$.

case	Q	Ra	Nu	Re	Δt	$N_x \times N_y \times N_z$
g1	10^8	6×10^9	10.29 ± 0.07	411.91 ± 4.75	2×10^{-8}	$192 \times 192 \times 72$
g2	10^8	1×10^{10}	15.93 ± 0.09	733.33 ± 5.85	2×10^{-8}	$384 \times 384 \times 96$
g3	10^8	2×10^{10}	27.60 ± 0.17	$1.44 \times 10^3 \pm 19.84$	2×10^{-8}	$384 \times 384 \times 144$
g4	10^8	4×10^{10}	48.05 ± 0.33	$2.87 \times 10^3 \pm 29.24$	2×10^{-8}	$768 \times 768 \times 144$
g5	10^8	8×10^{10}	82.63 ± 0.37	$5.56 \times 10^3 \pm 50.14$	2×10^{-8}	$768 \times 768 \times 192$

Table 7: **Details of the $Q = 10^8$ cases.** Δt is the timestep size. $N_x \times N_y \times N_z$ denotes the spatial resolution. The box ratio is $5\lambda_c \times 5\lambda_c \times 1$. The horizontal wavenumber $k_c = 41.1115$.

case	Q	Ra	Nu	Re	Δt	$N_x \times N_y \times N_z$
h1	2×10^6	2.1×10^7	1.048 ± 0.003	172.19 ± 2.15	1×10^{-6}	$96 \times 96 \times 48$
h2	2×10^6	2.5×10^7	1.386 ± 0.004	533.31 ± 10.77	1×10^{-6}	$192 \times 192 \times 48$
h3	2×10^6	2.7×10^7	1.56 ± 0.01	656.85 ± 13.08	1×10^{-6}	$192 \times 192 \times 48$
h4	2×10^6	3×10^7	1.81 ± 0.01	821.53 ± 19.56	1×10^{-6}	$192 \times 192 \times 48$
h5	2×10^6	4×10^7	2.63 ± 0.02	$1.40 \times 10^3 \pm 24.96$	1×10^{-6}	$192 \times 192 \times 48$
h6	2×10^6	5×10^7	3.38 ± 0.03	$1.89 \times 10^3 \pm 55.04$	1×10^{-6}	$192 \times 192 \times 48$
h7	2×10^6	7×10^7	4.68 ± 0.05	$2.82 \times 10^3 \pm 68.50$	5×10^{-7}	$288 \times 288 \times 72$
h8	2×10^6	1×10^8	6.36 ± 0.06	$4.13 \times 10^3 \pm 72.28$	1×10^{-7}	$576 \times 576 \times 144$
h9*	2×10^6	1.5×10^8	8.61 ± 0.08	$5.82 \times 10^3 \pm 85.70$	5×10^{-9}	$384 \times 384 \times 144$
h10*	2×10^6	1.7×10^8	9.33 ± 0.12	$6.31 \times 10^3 \pm 128.81$	1×10^{-9}	$768 \times 768 \times 288$

Table 8: **Details of the $Pr = 0.025, Q = 2 \times 10^6$ cases.** Δt is the timestep size. $N_x \times N_y \times N_z$ denotes the spatial resolution. The box ratio is $10\lambda_c \times 10\lambda_c \times 1$ in cases without *, and $5\lambda_c \times 5\lambda_c \times 1$ in cases with * above. The horizontal wavenumber $k_c = 18.9823$.
